Quantum ergodicity and scrambling in quantum annealers

Manuel H. Muñoz-Arias[1, *] and Pablo M. Poggi[2, †]

[1]*Institut Quantique and Département de Physique,*
Université de Sherbrooke, Sherbrooke, Quebec, J1K 2R1, Canada
[2]*Department of Physics, SUPA and University of Strathclyde, Glasgow G4 0NG, United Kingdom*
(Dated: November 20, 2024)

Quantum annealers play a major role in the ongoing development of quantum information processing and in the advent of quantum technologies. Their functioning is underpinned by the many-body adiabatic evolution connecting the ground state of a simple system to that of an interacting classical Hamiltonian which encodes the solution to an optimization problem. Here we explore more general properties of the dynamics of quantum annealers, going beyond the low-energy regime. We show that the unitary evolution operator describing the complete dynamics is typically highly quantum chaotic. As a result, the annealing dynamics naturally leads to volume-law entangled random-like states when the initial configuration is rotated away from the low-energy subspace. Furthermore, we observe that the Heisenberg dynamics of a quantum annealer leads to extensive operator spreading, a hallmark of quantum information scrambling. In all cases, we study how deviations from chaotic behavior can be identified when analyzing cyclic ramps, where the annealing schedule is returned to the initial configuration.

I. INTRODUCTION

The goal of exploiting quantum effects to solve computational problems more efficiently than classical devices has led to the fast-paced development of quantum technologies. A remarkably simple, yet potentially powerful, approach is quantum annealing [1], which uses adiabatic quantum evolution to tackle problems in combinatorial optimization. More broadly, adiabatic dynamics can be leveraged to perform universal quantum computation [2], in quantum control protocols for entangled-state preparation [3], and is closely related to variational quantum algorithms like the quantum approximate optimization algorithm (QAOA) [4, 5].

From a many-body physics perspective, the richness of adiabatic dynamics arises from the interplay between interactions and time-dependent driving. Interestingly, generic quantum many-body systems, in absence of extensive symmetries, are typically quantum chaotic [6–10], displaying features such as random-matrix-like spectral statistics [9], pseudorandom eigenstates [11–13], fast dynamical generation of entanglement [14], and three-stage dynamics in the entanglement spectrum [15]. The addition of driving and the ensuing lack of energy conservation typically enhances the dynamical signatures of chaos [16], and can turn integrable systems into chaotic ones [17].

In this context, adiabatic driving can be regarded as the "gentlest" form of time-dependence, as the slow change in system parameters leads to a quasi-static connection between eigenstates of different Hamiltonians. In generic many-body systems, however, such connection can only realistically be achieved in the low-energy

regime, where states can be protected by a sufficiently large energy gap. This suffices to guarantee the functioning of a quantum annealer, which focuses on ground states. But, the dynamical properties of these systems at other energy scales will be determined by a nontrivial interplay between driving, (non)adiabaticity, and chaos. So far, this regime has remained largely unexplored in the literature.

In this paper we explore many-body adiabatic evolution beyond the low-energy sector. We consider a system of spin-$\frac{1}{2}$ particles whose Hamiltonian is slowly interpolated between two integrable models through a chaotic path. This is the typical scenario in quantum annealing, where the system is driven from a "mixer" (noninteracting) Hamiltonian H_{M} at $t = 0$ to a "problem" (classical) Hamiltonian H_{P} at $t = T$, as depicted in Fig. 1a and 1b. We first explore the dynamics of the system when the initial product state is rotated away from the ground state of H_{M}, by studying the entanglement properties of the final state after the "anneal", $|\psi(T)\rangle$. Then, we probe global properties of the adiabatic evolution by analyzing properties of the unitary operator $U(t)$ dictating the full dynamics, for which we use standard diagnostics of quantum chaos based on the spectrum of eigenphases and eigenvectors of $U(t)$. Finally, we study the dynamics of generic operators in the Heisenberg picture through the formalism of operator growth and demonstrate the onset of quantum information scrambling.

The emergence of chaotic properties in the dynamics of a quantum annealer can be readily observed in a simple example shown in Fig. 1c. There, we plot the half-chain entanglement entropy the state $|\psi(T)\rangle$ at the end of the annealing schedule, as a function of the mean energy $\langle H_{\mathrm{M}}\rangle$ of the initial product state for different system sizes N. For $\langle H_{\mathrm{M}}\rangle = \pm N$, the initial state is the ground state of $\pm H_{\mathrm{M}}$, i.e. the standard annealing scenario, and in consequence we obtain that the corresponding final
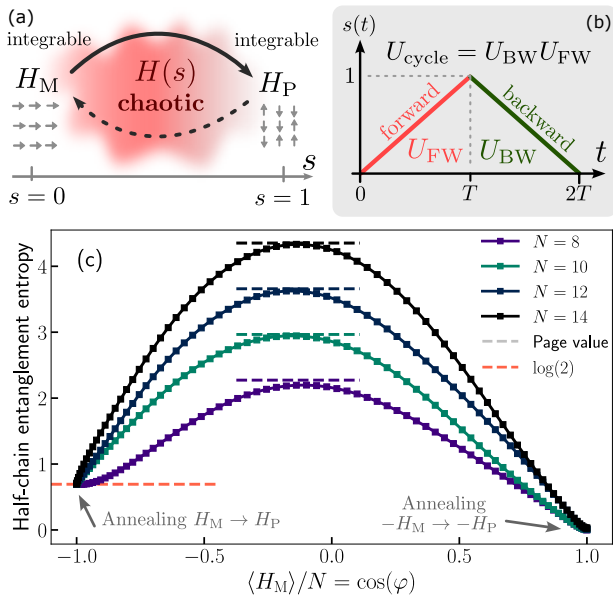
FIG. 1. (a) Schematic of a quantum annealing protocol. Two integrable Hamiltonians H_M and H_P are interpolated by chaotic Hamiltonian $H(s)$. Slowly varying the parameter s from 0 to 1 will connect the ground state of H_M to that of H_P. (b) The forward ramp from $s(t=0)=0$ to $s(t=T)=1$ leads to the unitary map $U(T) \equiv U_{FW}$. Ramping back from $s=1$ to $s=0$ generates the backwards unitary U_{BW} such that the cyclic process is given by $U_{cycle} = U_{BW}U_{FW}$. (c) Half-chain entanglement entropy of the state $|\psi(T)\rangle$ at the end of a forward ramp under annealing dynamics, for the Ising model described in Sec. II. The initial state is the spin coherent state $|\psi(0)\rangle = |\theta=0, \varphi\rangle$, where all qubits are pointing along the direction $(\cos(\varphi), \sin(\varphi), 0)$ on the Bloch sphere. For $\varphi \to 0, \pi$, the dynamics connects the ground state of $\pm H_M$ to that of $\pm H_P$ and generate little entanglement. For intermediate values of φ, the final states acquire volume-law entanglement entropy, similar to that of random states.

states are only slightly entangled. However, as the initial state is rotated away from the ground state (by angle φ, as described in Sect. III) we find that the final configuration acquires a entanglement entropy which grows with system size. At the peak, the final states exhibit clear volume-law entanglement entropy, well approximated by Page's value [18]. We thus observe that the annealing dynamics is generating random-like states with very high entanglement, akin to what is expected from the time evolution of a fully quantum chaotic system.

As we show in this paper, the observed chaotic features turn out to be generic and emerge in the dynamics of most initial states. Interestingly, we find that significant deviations from chaoticity are observed if one considers a cyclic annealing schedule, where the interpolation parameter $s(t)$ is driven from $s(t=0)=0$ to $s(t=T)=1$ and then back to $s(t=2T)=0$; see Fig. 1 (b). For such case, we observe the existence of eigenstates of $U(2T)$ that show clear signatures of low-energy states, in par-

ticular displaying area-law entanglement, and that the dynamics of global operators show unscrambling features.

The rest of the manuscript is organized as follows. In Sec. II we introduce the model we use in this paper, characterize the onset of chaos and integrability for different parameter values, and discuss the connection between adiabaticity and the spectral gaps throughout the energy spectrum. In Sec. III we analyze the evolution of initial states that are rotated away from the ground state of H_M. Expanding on the example discussed in Fig. 1 and considering both forward and cyclic adiabatic ramps. In Sec. IV we study properties of the many-body time-evolution operator $U(t)$ describing the dynamics. We focus on the analysis of the statistical properties of its eigenphases and entanglement structure of its eigenstates. We connect the behavior of these quantities to the emergence of chaotic signatures in the system for both forward and cyclic driving protocols. In Sec. V we study the adiabatic dynamics of the system in the Heisenberg picture. For that, we consider different sets of initial operators and probe the emergence of quantum information scrambling by tracking how the mean operator size evolves in time for the two driving protocols. Finally, in Sec. VI we summarize our findings, discuss how our results could inform new uses and applications of quantum annealers, and propose potential avenues for future work.

II. PHYSICAL MODEL AND DRIVING PROTOCOL

We consider a system of N spin-$\frac{1}{2}$ particles described by a Hamiltonian of the form

$$H(s) = sH_M + (1-s)H_P, \qquad (1)$$

where

$$H_M = \sum_{i=1}^{N} \sigma_i^x \qquad (2)$$

$$H_P = \sum_{i,j=1}^{N} \chi_{ij}\sigma_i^z\sigma_j^z + \sum_{i=1}^{N} \lambda_i\sigma_i^z \qquad (3)$$

and where $\{\sigma_i^\alpha\}$ with $\alpha = x, y, z$ denote the usual Pauli operators acting on site $i = 1, \ldots, N$. The parameter $s \in [0, 1]$ allows to interpolate between the noninteracting mixer Hamiltonian H_M, and the interacting classical Hamiltonian H_P which is diagonal in the computational basis for any choice of connectivity $\{\chi_{ij}\}$ and local longitudinal fields $\{\lambda_i\}$. The problem Hamiltonian H_P can encode instances of quadratic binary optimization (QUBO) problems [19] for instance maximum cut and maximum independent set [20], as well as describe physical models of relevance to the theory of spin glasses and statistical mechanics [21, 22]. In this work we focus entirely on the simplest scenario, where interactions are nearest-neighbor $\chi_{ij} = \delta_{j,i+1}$ (with open boundary conditions) and the local field is homogeneous across all sites
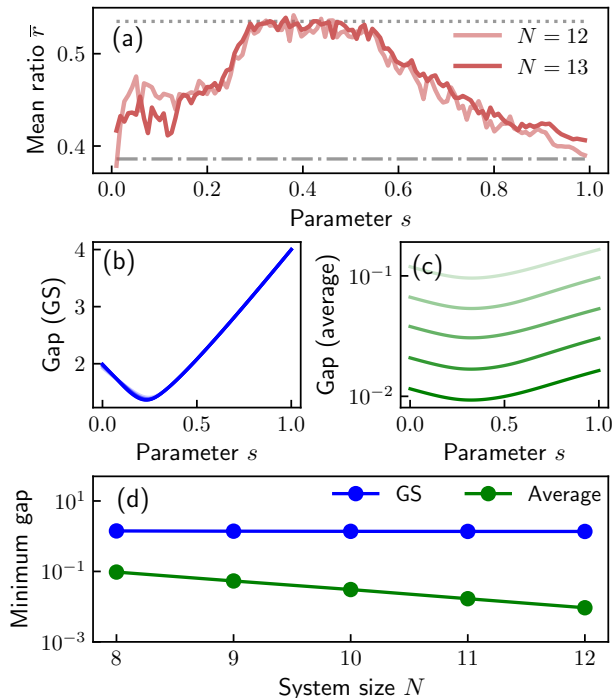
FIG. 2. Spectral properties of Hamiltonian $H(s)$ in Eq. (1). (a) Mean level spacing ratio $\bar{r}$, defined from Eq. (5), as a function of the interpolation parameter s. Average is taken over the bulk of the spectrum, here defined by not considering the top 5% lowest and highest energy levels. Dotted (dash-dotted) lines indicate the values of $\bar{r}$ for chaotic (GOE) and integrable (Poisson) models. (b) and (c) Spectral gaps as a function of s for system sizes $N \in [8, 12]$ (light to dark tones). Figure (b) shows the ground state gap $\Delta_0(s)$, while (c) shows the average gap $\sum_j \Delta_j/(\tilde{d} - 1)$ with $\tilde{d}$ the relevant Hilbert space dimension. (d) Scaling of the minimum ground state gap and average gap with system size N; minimum is taken over $s \in [0, 1]$. All calculations are performed in the positive parity sector of the Hamiltonian $H(s)$, whose dimension is $d = 2^{N-1}$.

$\lambda_i = \lambda = 1$. This choice makes $H(s)$ in Eq. (1) equivalent to the mixed-field Ising model [23–25].

The Hamiltonian in Eq. (1) is trivially integrable for $s = 0$ and $s = 1$, while for $s \in (0, 1)$ integrability is broken and the model becomes quantum chaotic. As discussed in Ref. [26], a similar situation is found for most choices of connectivity graphs χ_{ij} (at least, those far from the disconnected and completely connected regimes). This motivates our choice of the nearest-neighbor graph as a simple representative of the typical case leading to a chaotic path interpolating between two integrable limits, as depicted in Fig. 1a. The onset of chaos can be diagnosed by the emergence of level repulsion in the bulk of the energy spectrum of the Hamiltonian, which in turn can be quantified by the mean level spacing ratio (MLSR) $\bar{r}$ [27]. Given a set of eigenvalues $\{e_i\}$, the associated level

spacings (gaps) are

$$\Delta_j = e_{j+1} - e_j \tag{4}$$

and we define the spacing ratios as

$$r_j = \frac{\max(\Delta_j, \Delta_{j+1})}{\min(\Delta_j, \Delta_{j+1})}. \tag{5}$$

The MLSR is computed as the mean of the set $\{r_j\}$ across the bulk of the spectrum. For quantum chaotic Hamiltonians, the MLSR matches random matrix theory predictions; for the case of the model considered here, the relevant matrix ensemble is the Gaussian Orthogonal Ensemble for which $\bar{r}_{\text{GOE}} \simeq 0.535$ [27]. Integrable systems show uncorrelated level statistics yielding $\bar{r}_{\text{INT}} \simeq 0.386$ [27]. Importantly, for the MLSR (and any other spectral property) to be meaningful one must consider a given symmetry sector of the Hamiltonian. For the model in Eq. (1), the only discrete symmetry present is related to the invariance of the system when performing a reflection with respect to the middle of the chain. We choose to work in a positive parity sector since this is where the ground state of H_{M} resides.

In Fig. 2 (a) we plot the MLSR $\bar{r}$ for the Hamiltonian in Eq. (1) as a function of the interpolation parameter s for the chosen geometry. Dotted (dash-doted) lines indicate expected limiting values for chaotic (integrable) models. We observe that the model is maximally chaotic for $s \simeq 0.3 - 0.6$, with clear deviations from the GOE predictions as $s = 0$ and $s = 1$ are approached. We emphasize that this characterization of quantum chaos corresponds to the static Hamiltonian $H(s)$ where s is fixed. Nonetheless, these results will inform our analysis of the properties of the adiabatically-driven system in the next sections.

A. Gap characterization and adiabaticity

We are interested in analyzing the dynamics of the system when the parameter $s = s(t)$ is slowly changed in time. We consider two protocols: a standard *forward* ramp, and a *cyclic* ramp. In the forward ramp, $s(t) = t/T$ and the Hamiltonian is interpolated between H_{M} at $t = 0$ to H_{P} at $t = T$. This is the usual scenario in quantum annealing where one expects to connect the ground state of H_{M} to that of H_{P}. In the cyclic ramp, on the other hand, $s(t) = t/T$ for $t \in [0, T]$ and $s(t) = (2T - t)/T$ for $t \in (T, 2T]$, such that the Hamiltonian returns to H_{M} at the final time $t = 2T$. In this case, the system initially prepared in one of the eigenstates of H_{M} will return to the same eigenstate at $t = 2T$ if the evolution is truly adiabatic, having acquired an overall geometric phase in the process [28].

A key aspect of designing the adiabatic driving is to make sure that the conditions of the Adiabatic Theorem are met throughout the evolution. For $H(s) = H(s(t))$

and $s \sim t/T$, these can be roughly translated into the requirement [29, 30].

$$T \gg \max_{s \in [0,1]} \frac{|\langle k| \frac{\partial H}{\partial s} |n\rangle|}{\Delta_n(s)^2} \qquad (6)$$

where $|n\rangle$ and $|k\rangle$ denote instantaneous eigenstates of $H(s)$ and $\Delta_n(s)$ is the spectral gap of Eq. (4). In a generic many-body system, however, the exponential amount of energy levels in a given fixed energy window (in the bulk of the spectrum) precludes the validity of Eq. (6) for the entirety of the spectrum even for moderate system sizes. For the model we consider this can be seen by analyzing the scaling of the spectral gaps $\Delta_j(s)$ defined in Eq. (4). In Fig. 2b and 2c we plot the ground state gap $\Delta_0(s)$ and the average gap

$$\overline{\Delta}(s) = \frac{1}{\tilde{d}-1} \sum_{j=1}^{\tilde{d}} \Delta_j(s), \qquad (7)$$

where $\tilde{d}$ indicates the dimension of the positive parity subspace, $d \simeq 2^{N-1}$. Curves are shown for various system sizes $N \in [8, 12]$, revealing that the ground state gap remains finite as the system is scaled up, while the average gap shrinks exponentially. This is confirmed by the data in Fig. 2 (d) which shows the scaling of the minimum values of $\Delta_0(s)$ and $\overline{\Delta}(s)$ with system size. These results show that in order to strictly meet the adiabaticity condition Eq. (6) for every energy level, the evolution time would have to grow exponentially with system size, making it practically unfeasible.

This effective lack of adiabaticity in a many-body system is not surprising, and it can be seen as a consequence of the exponential growth of Hilbert space dimension (nonetheless, see Ref. [31, 32] for important exceptions). Here we take the approach of considering evolution times T that are long enough to meet condition (6) for the low (and high) energy portions of the spectrum - in particular for the ground state of the system. These are the conditions in which quantum annealers are ideally designed to work in. Our focus will be in analyzing the dynamical process *as a whole*, without restricting to analyzing only the evolution of the ground state.

III. EVOLUTION OF SPIN COHERENT STATES

In this section we explore the dynamics of different states under the slow adiabatic driving. Formally, the annealing dynamics is described by the set of unitaries

$$U(T_{\text{tot}}) := \mathcal{T}\left[e^{-i \int_0^{T_{\text{tot}}} dt H(s(t))} \right] \qquad (8)$$

with $\mathcal{T}[.]$ the time ordering operator, $T_{\text{tot}} = T, 2T$ for the forward and cyclic ramps, respectively, and $s(t)$ chosen accordingly. In our numerical simulations we approximate the ideal protocol with a discretized version of the

form

$$U(T_{\text{tot}}) \approx \prod_{m=0}^{q-1} e^{-im\Delta t H(s(m\Delta t))}, \qquad (9)$$

with Δt the time step and $q = T_{\text{tot}}/\Delta t$ the total number of steps. Hence, the protocol is controlled by the two independent parameters $(\Delta t, T_{\text{tot}})$, which can always be chosen to guarantee the fulfillment of the adiabatic condition (for the low energy sector). Here, we take $T_{\text{tot}} \propto N^2$ [33, 34] and $\Delta t < 1$ [35, 36], which satisfy the above requirements.

We begin our exploration of the quantum ergodic properties in the annealing process by considering the evolution of product states where initially all spins are polarized along the same direction $\vec{n}$, such that

$$|\psi(0)\rangle = |\uparrow_{\vec{n}}\rangle^{\otimes N} = |\theta, \varphi\rangle \qquad (10)$$

are spin coherent states (SCS) [37], where $\vec{n}$ is defined by the polar and azimuthal angles (θ, φ). Note that $|\pi/2, \pi\rangle = |\psi(0)\rangle = |-\rangle^{\otimes N}$ and $|\pi/2, 0\rangle = |\psi(0)\rangle = |+\rangle^{\otimes N}$ are the lowest and highest energy eigenstates of H_{M}, respectively. We define a continuous family of SCSs connecting these two extremal states as

$$\mathcal{S} = \{|\pi/2, \varphi\rangle \mid \varphi \in [0, \pi]\}, \qquad (11)$$

which cover the full range of energies of H_{M} since $\langle H_{\text{M}}\rangle = \langle \pi/2, \varphi|H_{\text{M}}|\pi/2, \varphi\rangle = N \cos(\varphi)$. For the results discussed in this section we always take $|\psi(0)\rangle \in \mathcal{S}$.

For both the forward and cyclic protocols we investigate the ergodicity of the evolution by computing the half-partition entanglement entropy of the final state. This quantity measures the degree of entanglement between two subsets A and B in a collection of N spins, with $|A \cup B| = N$. Given a pure state $|\psi\rangle$ of the N spins, the reduced density matrix of the subsystem A (respectively, B) $\rho_A = \text{tr}_B(|\psi\rangle\langle\psi|)$ associated with the considered bipartition gives access to the half-partition entanglement entropy as the von Neumann entropy of the reduced state

$$S_A = -\text{tr}\left(\rho_A \log(\rho_A)\right) = -\sum_l \lambda_l \log(\lambda_l), \qquad (12)$$

where $\{\lambda_l\}_{l=1,\dots,2^{|A|}}$ are the eigenvalues of ρ_A satisfying $\sum_l \lambda_l = 1$. For the rest of the manuscript we fix A as the block of the $N/2$ left-most spins in the chain and B the complement, and thus we will refer to the quantity in Eq. (12) as half-chain entanglement entropy. Typically, time evolution under a time-independent chaotic Hamiltonian or chaotic unitary transforms initial product states, with $S_A = 0$, into highly entangled states which are indistinguishable from random pure states with S_A saturating the Page value $S_A \sim \frac{\log(2)}{2} N$ [18].

A. Forward ramps

First, we consider the evolution of every state $|\psi(0)\rangle \in \mathcal{S}$ with a forward ramp and compute S_A of the final state
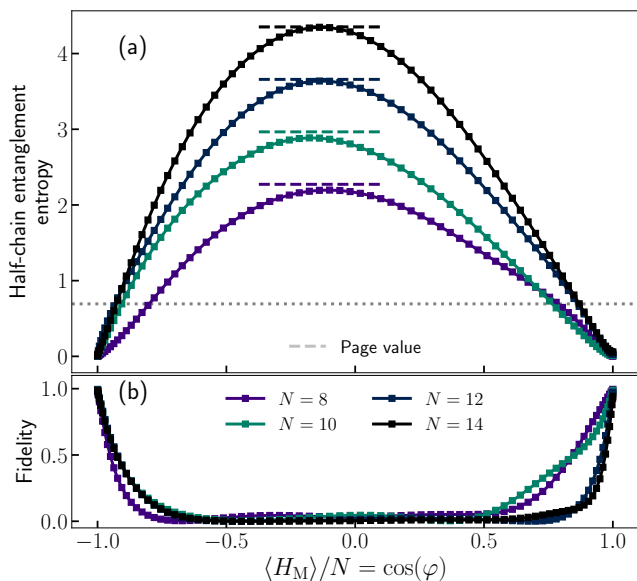
FIG. 3. Properties of the final state, $|\psi(2T)\rangle$, for a cyclic ramp initialized with a spin coherent state pointing along the direction given by angles $(\theta, \varphi) = (\pi/2, \varphi)$ (see main text for details), for systems $N = 8, 10, 12, 14$. (a) Half-chain entanglement entropy S_A of $|\psi(2T)\rangle$ as a function of the mean-energy density of the initial state which is determined by its direction. The dashed lines indicate the Page value for the respective system size. The dotted line indicates $S_A = \log(2)$. (b) Fidelity between initial and final states of the cyclic ramp as function of the initial state mean-energy density. A perfect cyclic evolution is characterized by a unit fidelity. Only states with a small mean-energy density neighborhood of either $|+\rangle^{\otimes N}$ and $|-\rangle^{\otimes N}$ can be successfully returned to their initial configuration. Parameters are: $T = 600$, $\Delta t = 0.05$.

$|\psi(T)\rangle$. When $|\psi(0)\rangle = |\pi/2, \pi\rangle$ with $\langle H_M \rangle / N = 1$, this is the standard quantum annealing scenario. Naturally, the ground state of H_P is reached at the end of the ramp, as is witnessed by the value $S_A = \log(2)$ in Fig. 1c (orange dashed line). The opposing limit, where $\varphi = 0$ and $\langle H_M \rangle / N = -1$, can be regarded as an anneal between $-H_M$ and $-H_P$, for which the final state is a product state and so $S_A = 0$, as also seen in the Figure.

For initial states away from the two extremal cases, we find that they reach final configurations with S_A rapidly converging to the Page value of random pure states (colored dashed lines in Fig. 1c). Interestingly, states with S_A closer to the Page value also have mean-energy $\langle H_M \rangle \approx 0$, corresponding with the middle of the energy spectrum, an observation which will be further discussed in Sec. IV. Finally, since $\langle \theta, \varphi | H_M | \theta, \varphi \rangle = N \sin(\theta) \cos(\varphi)$, all other $|\theta, \varphi\rangle \notin \mathcal{S}$ have a mean-energy which rapidly decreases away from $\theta = \pi/2$. Hence the fate of the majority of states, $|\theta, \varphi\rangle$, in the manifold of SCSs, with the exception of small neighborhoods in the vicinity of $(\theta, \varphi) = (\pi/2, 0), (\pi/2, \pi)$, i.e., $\langle H_M \rangle / N = \pm 1$, is to be transported by the forward ramp into highly entangled states, displaying an entanglement entropy which grows

with system size, and with some of them resembling random pure states.

B. Cyclic ramps

We now consider the cyclic ramp. For a perfect adiabatic connection, the two extremal states, $|\pi/2, 0\rangle = |+\rangle^{\otimes N}$ and $|\pi/2, \pi\rangle = |-\rangle^{\otimes N}$, must be transported into themselves, i.e., $|\psi(2T)\rangle = |\psi(0)\rangle = |\pi/2, \{0, \pi\}\rangle$. Hence, we are also interested in determining the degree to which such return takes place. To do so, we look at the final state fidelity $f(2T) = |\langle \psi(2T)|\psi(0)\rangle|^2$, which will complement the study of the entanglement entropy S_A.

Both $S_A(2T)$ and $f(2T)$ for all $|\psi(0)\rangle \in \mathcal{S}$ are shown, as function of the mean-energy density $\langle H_M \rangle / N$ of the initial state, in Fig. 3a and 3b, respectively. We find that the two extremal states of H_M are successfully connected back to themselves through the cyclic evolution, as evidence by the corresponding values of $S_A(2T) = 0$ and $f(2T) = 1$. On the other hand, most of the initial states reach "warmer" states, i.e., $S_A(2T) > 0$. In particular, the value of $S_A(2T) = \log(2)$ (grey dotted line in Fig. 3a) seems to provide a good discriminator between initial states reaching $f(2T) > 0$ and $f(2T) \sim 0$ when $S_A(2T) < \log(2)$ or $S_A(2T) > \log(2)$, respectively. Furthermore, most of the energy range defined by H_M is occupied by states which fail to come back to themselves with a finite $f(2T)$. In connection with the above discriminator, we see that states with $S_A(2T) < \log(2)$ have $|\langle H_M \rangle / N| \gtrsim 0.9$ and those with $S_A(2T) > \log(2)$ have $|\langle H_M \rangle / N| \lesssim 0.9$. Notice that the effect is also asymmetric: It is easier to transport along a cyclic adiabatic ramp product states with $\langle H_M \rangle$ close to the top of the spectrum than those with $\langle H_M \rangle$ close to the bottom of the spectrum of H_M.

Finally, we stress that the results discussed in Sec. III A and Sec. III B are not unique to product states; in fact, entangled initial states display a similar behavior. In App. A we report results for a set of initial states given by the eigenstates of H_M, i.e., Dicke states, which are in general entangled. This suggests an initial-state-independet character of the reported behavior, connected to universal properties of the unitary operator $U(T_{tot})$. We explore this aspect of the problem in the following section.

IV. CHAOS IN THE UNITARY EVOLUTION OPERATOR

In this section we characterize the global spectral properties of the unitary evolution operator describing the adiabatic driving of the Hamiltonian in Eq. (1), as approximated by Eq. (9). We investigate the onset of quantum chaos on the annealing process from properties of the eigenphases and eigenvectors of $U(t)$.

The degree of correlation among eigenphases is studied with the MLSR as introduced in Eq. (4) and Eq. (5),
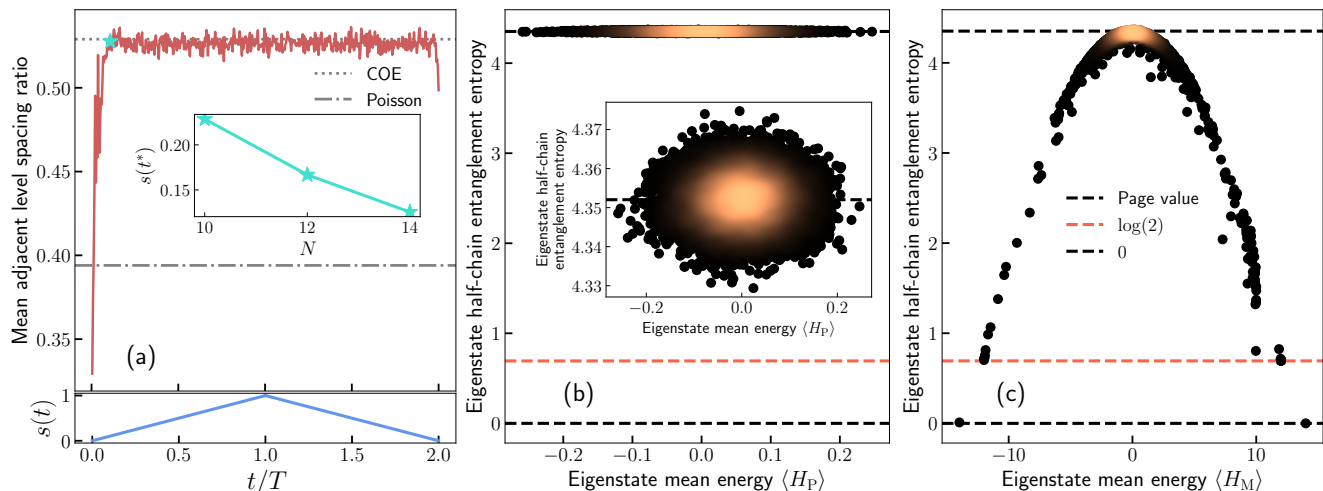
FIG. 4. Spectral properties of the adiabatic unitary operator for both forward and cyclic ramps. (a) Mean level spacing ratio (MLSR) as a function of time for $0 \leq t \leq 2T$ covering both forward and backward ramps. The green star indicates the first time instant t^* at which the unitary becomes fully chaotic ($s \simeq 0.14$ for $N = 14$), and the inset shows the behavior of this quantity with system size. The dash-dot line shows the MLSR for an integrable system and the dotted line that of a chaotic system. The bottom panels shows $s(t)$, with the forward ramp stopping at $t/T = 1$ and the cyclic ramp defined over the full range of t/T. (b) Half-chain entanglement entropy of all the eigenstates of $U(T)$ as a function of their mean energy with respect to the problem Hamiltonian H_{P}. (c) Half-chain entanglement entropy of all the eigenstates of $U(2T)$ as a function of their mean energy with respect to mixer Hamiltonian H_{M}. Both in (b) and (c) the dots are colored based on the local density, with black indicating very low density and light orange indicating very high density, the dashed lines (bottom to top), indicate $\mathcal{S} = 0, \log(2), 0.5\log(N) - 0.5$, respectively. In all panels the parameters are: $N = 14$, $T = 600$, $dt = 0.5$.

allowing us to discern whether the unitary can be associated with an integrable, quasi-integrable, or quantum chaotic system. As we deal with spectral properties of a unitary operator, the random matrix ensembles linked with quantum chaotic behavior are now the circular ensembles [38]. In particular, for the circular orthogonal ensemble (COE), $\bar{r}_{\mathrm{COE}} \simeq 0.529$. In contrast with the case of Hamiltonian spectra, unitary operators do not have a clear-cut notion of low-energy and bulk sectors in their spectra. As such, we perform the MLSR analysis including *all* the eigenphases of the positive parity symmetry sector.

To study the structure of the eigenstates, we use the half-partition entanglement entropy S_A as defined un Eq. (12). For many-body systems in one dimension the half-chain entanglement entropy of individual eigenstates as a function of system size displays two dominant behaviors: i) Area-law entanglement with $S_A(N) \simeq K$ with K a constant independent of the system size, and ii) volume-law entanglement with $S_A(N) = c_1 N + c_2 + O(N^{-1})$ a linear dependence on the system size. The coefficients $c_{1,2}$ allow us to distinguish between random gaussian states [39, 40] and random pure states which saturate the Page value [18], with $c_1 = \log(2)/2$ and $c_2 = -1/2$. Importantly, chaotic eigenstates of many-body Hamiltonians obey a volume-law of the half-chain entanglement entropy [13, 41, 42], thus one can diagnose the presence of this type of eigenstates based on the behavior of S_A.

A. Forward ramps

The evolution along the forward ramp is defined iteratively via a product of unitaries in time succession, see Eq. (9). For $t = m\Delta t \in [0, T]$, we write $U(t = m\Delta t) = \left[\prod_{p=0}^{m-1} e^{-ip\Delta t H(s(p\delta t))} \right] e^{-im\Delta t H(s(m\Delta t))}$ where the product inside the square brackets is the unitary up to the preceding time $U((m-1)\Delta t)$. The unitary of the full ramp is obtain when the number of steps equals $T/\Delta t$. The spectral decomposition of any of the unitaries along the ramp reads $U(t)|\mu_l(t)\rangle = e^{-i\mu_l(t)}|\mu_l(t)\rangle$, with $\{\mu_l(t)\}_{l=1,..,2^N}$ the set of eigenphases and $\{|\mu_l(t)\rangle\}_{l=1,..,2^N}$ the set of associated eigenvectors, and with $t \to T$ for the unitary of the full evolution $U(T)$.

We consider first the MLSR of the set of eigenphases $\{\mu_l(t)\}$ of each of the unitaries $U(t)$ for $0 \leq t \leq T$, i.e., along the ramp. The results are shown in Fig. 4a for a system with $N = 14$ spins. Naturally, at $s(t \simeq 0)$ the MLSR indicates the global properties of the unitary coincide with those of an integrable system, which is expected given that $H(s(0)) = H_{\mathrm{M}}$. Nonetheless, we find that once the ramp $s(t)$ reaches a value as small as $s(t^*) \simeq 0.14$ (green star in in Fig. 4a), the unitary already shows a MLSR agreeing with that of a COE random matrix, indicating the evolution has become quantum chaotic. Note that at that point in the interpolation path ($s \simeq 0.14$), the instantaneous Hamiltonians $H(s)$ are still far from the fully chaotic regime, as can be seen from Fig. 2a. Interestingly, analyzing $s(t^*)$ vs N shows a clear decreasing

tendency with increasing N (see inset in Fig. 4a). Thus, we observe that even the 'gentle' adiabatic driving has a notable effect by leading to an early emergence of ergodic properties in the unitary evolution operator. Further, we observe that for the rest of the forward ramp, *i.e.*, $s(t^*) < s(t) < 1$, the adiabatic evolution unitary remains quantum chaotic.

Having observed the emergence of chaotic properties along the forward ramp as witnessed by the properties of the eigenphases, we now focus on the unitary of the complete forward ramp, $U(T)$, and its associated set of eigenstates $\{|\mu_l(T)\rangle\}_{l=1,..,2^N}$. In Fig. 4b we plot the half-chain entanglement entropy of all eigenstates of $U(T)$ as a function of their mean energy with respect to H_P, the Hamiltonian at the end of the forward ramp. As anticipated by the MLSR analysis, the forward ramp leads to spectral properties of the unitary coinciding with those of a COE random matrix, thus most eigenstates have a S_A which is consistent with the Page value for random pure states. We emphasize that there is no dependence on the final energy, i.e. we observe no signatures of the presence of a low energy or high energy sectors. The inset shows a closer view of the values of S_A where a Gaussian distribution centered at $(\langle H_P \rangle, S_A) = (0, 7\log(2) - 1/2)$ is apparent. Thus, our analysis shows that the dynamical map $U(T)$ describing the adiabatic evolution is highly chaotic, and spectrally indistinguishable from a random quantum circuit.

B. Cyclic ramps

The onset of quantum chaos becomes more subtle (and thus, more interesting) when we consider the evolution along the cyclic ramp. Since the cyclic ramp is composed of a forward and a backward ramps, the first half of the evolution is always described by $U(T)$. Hence, the results of the MLSR study discussed in Sec. IV A apply here for the first half of the evolution. For the second half of the evolution completing the cyclic ramp, the results of the MLSR analysis are shown in the same Fig. 4a, for the regime $T \leq t \leq 2T$. We notice that for most of the backward ramp the chaotic properties remain and only for the final portion, $s(t) \gtrsim 1.9$, we observe a deviation from the COE value, with the MLSR of the eigenphases of $U(2T)$ acquiring an intermediate value between $\bar{r}_{\text{Int}}$ and $\bar{r}_{\text{COE}}$. Thus, while there is still some degree of level repulsion, the system no longer resembles a fully random unitary. In fact, subsets of the eigenphases can unambiguously be labeled as low- and high-energy, and bulk. This means that the spectral structure of $U(2T)$ is more similar to that of a Hamiltonian system, than of a random unitary. We devote the rest of this section to a judicious quantitative study supporting our previous claim.

Recall that for a time-independent many-body Hamiltonian the entanglement entropy S_A of eigenstates allows us to distinguish ergodic (S_A saturating the Page value) from nonergodic (S_A constant) eigenstates. Typically
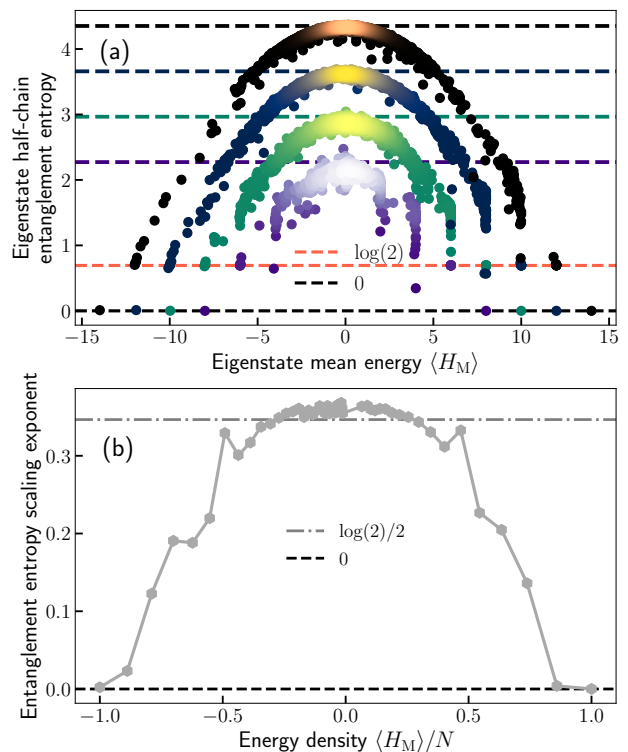

FIG. 5. (a) Half-chain entanglement entropy of all the eigenstates of $U(2T)$ as function of their mean energy with respect to H_P. Darker color indicates low point density, lighter color indicate high point density. Purples, greens, blues, black, correspond to system sizes of $N = 8, 10, 12, 14$, respectively. The bottom two dashed lines indicate $\mathcal{S} = 0, \log(2)$, the top four dashed lines indicate the Page value of the entanglement entropy for the respective system size. (b) Scaling exponent with system size of the locally averaged half-chain entanglement entropy. A rapid convergence to the Page value of $\log(2)/2$ indicates that most of the eigenstates considered in (a) exhibit volume-law entanglement entropy and thus are ergodic states.

a quantum chaotic Hamiltonian has eigenstates of both types, with nonergodic ones constituting a small fraction appearing close to the lower and top ends of the energy spectrum, and ergodic ones constituting the dominant fraction which cluster close to the middle of the energy spectrum [13].

We thus focus on $U(2T)$ and ask: how similar is the structure of its eigenstates $\{|\mu_l(2T)\rangle\}_l$ as seen in the plane $(\langle H_M \rangle, S_A)$ to that of a chaotic Hamiltonian? Here $H_M = H(0) = H(2T)$ defines the natural energy scale. In Fig. 4c we show S_A of all the $\{|\mu_l(2T)\rangle\}_l$ as function of their mean energy $\langle H_M \rangle$ for a system of $N = 14$ spins. This way of displaying S_A unveils a structure with strike similarity to that of a nonintegrable (quantum chaotic) Hamiltonian [13], in stark contrast with the expectation that the cyclic ramp must recover the structure of the integrable initial Hamiltonian H_M. Further, the structure seen in Fig. 4c shows clear emergent energy sectors

which can be classified into low-energy, bulk, and high-energy, distinctions which are absent in the forward-ramp unitary.

The lack of adiabaticity in the bulk of the spectrum is evident in the preceding analysis. A system evolving in perfect adiabatic fashion should connect every eigenstate of H_M to itself after the cyclic ramp. Thus, in the S_A vs energy diagram, one would observe that only discrete values of $\langle H_\mathrm{M} \rangle$ are present (in this case, this would be $N + 1$ distinct eigenvalues). In contrast to this, we find the values of $\langle H_\mathrm{M} \rangle$ appear to be continuous in value, particularly near $\langle H_\mathrm{M} \rangle \approx 0$.

To complete our investigation of the structure of eigenstates of $U(2T)$, we look into the behavior of S_A as a function of the system size N. In Fig. 5a we show S_A vs $\langle H_\mathrm{M} \rangle$ for all the eigenstates of $U(2T)$ for systems with $N = 8, 10, 12, 14$ (purples, greens, blues, black, respectively). We find that, even for the smallest size considered, signatures of a structure resembling that of a nonintegrable Hamiltonian are noticeable. We thus study $S_A(N)$ in terms of an energy density $E_\mathrm{d} = \langle H_\mathrm{M} \rangle / N \in [-1, 1]$. We bin the E_d axis into small energy-density windows $E_\mathrm{W} = [E_\mathrm{d} - \Delta E_\mathrm{d}, E_\mathrm{d} + \Delta E_\mathrm{d}]$, whose size is chosen as to not have empty windows. For each system size we count the number of eigenstates inside a given energy-density window $N_\mathrm{W} = |\{S_A(\epsilon) : \epsilon \in E_\mathrm{W}\}|$ with $|.|$ indicating the cardinality of the set, and compute the energy-window averaged S_A, that is $\overline{S_A}\big|_{E_\mathrm{W}} = \frac{1}{N_W} \sum_{\epsilon \in E_\mathrm{W}} S_A(\epsilon)$. Finally we regress the energy-density window averaged S_A's to a linear model, that is, $\overline{S_A}\big|_{E_\mathrm{W}}(N) \leftarrow aN + b$ with (a, b) the regression coefficients.

In Fig. 5b we show the values of a as a function of E_d. We recognize two distinct behaviors, volume-law entanglement and area-law entanglement, with the particularity that the volume-law eigenstates can be subdivided into two different groups. For $|E_\mathrm{d}| < 0.5$ we can unambiguously conclude that the eigenstates of $U(2T)$ obey a volume-law of entanglement which is consistent with the Page result for random pure states, and that the majority of eigenstates are found in this region. For $0.5 < |E_\mathrm{d}| \lesssim 0.8$, we encounter few sets of eigenstates which do follow a volume-law of entanglement but whose values of (a, b) indicate they might be random Gaussian states [40]. Finally, for $|E_\mathrm{d}| > 0.8$ we observe four sets of eigenstates which obey an area-law of entanglement. Interestingly for all system sizes studied, we can readily recognize the states in this last category. Naturally, the lowest and highest energy states, at $E_\mathrm{d} = \pm 1$, correspond to the ground state $|-\rangle^{\otimes N}$ and highest excited state $|+\rangle^{\otimes N}$ of H_M, which appear both in Fig. 4c and Fig. 5a at $S_A = 0$ (first black dashed line). The next one, in increasing S_A, corresponds to Dicke states with one flip (low-energy) and $N - 1$ flips (high-energy), and states with similar entanglement structure, appearing at $S_A = \log(2)$ (orange dashed line) in Fig. 4c and Fig. 5a.

V. OPERATOR DYNAMICS AND INFORMATION SCRAMBLING

In this section we analyze the quantum annealing dynamics by focusing on the Heisenberg evolution of different classes of operators. In particular, we will study the size of operators as a function of time, which is a standard metric in the study of quantum information scrambling [43–46]. During scrambling dynamics, initially local operators expand towards the rest of the degrees of freedom of the system, in such a way that their support becomes increasingly nonlocal and the so-called mean operator size $\mu(t)$ (to be defined below) becomes extensive. For general unitary dynamics, this process can be described by the operator size distribution (OSD) $\{P_k(t)\}$, $k = 1, \ldots, N$, where $P_k(t) \geq 0$ and $\sum_k P_k(t) = 1$. For a given initial operator $A(0)$, $P_k(t)$ quantifies the support of the Heisenberg-evolved operator $A(t) = U(t)^\dagger A(0) U(t)$ in the set of Pauli operators $\{Q\}_{r(Q)=k}$ of size exactly k. Here the size $r(Q)$ of a multibody Pauli operator equates the Hamming weight of the associated Pauli string. Formally, the OSD is defined as

$$P_k(t) = \frac{1}{d^2 \, \mathrm{Tr}\,(A^2)} \sum_{r(Q)=k} |\mathrm{Tr}\,(Q\, U(t)^\dagger A U(t))||^2, \quad (13)$$

where $d = 2^N$. In turn, the mean operator size is defined as the first moment of this distribution,

$$\mu(t) = \sum_{k=1}^{N} k P_k(t). \quad (14)$$

Evidently, $1 \leq \mu(t) \leq N$. For local operators, one expects $\mu(t)$ to grow at short times (in some cases, exponentially [47]) and, under generic dynamics, the mean operator size becomes extensive, i.e., proportional to the system size N. Particularly, a Haar-random unitary leads to $\mu_\mathrm{Haar} \simeq 3N/4$ independent of our choice of initial Pauli operator. We point out that the properties of the mean operator size are tightly connected with that of out-of-time-ordered correlators, as discussed in Ref. [46]. Naturally, higher order moments of the OSD can also be considered as more refined descriptions of the scrambling process [43, 46].

We will consider the dynamics of two types of initial operators: single-site and global. Single-site operators correspond to size-one Paulis, e.g.

$$A(0) \to \{\sigma_{i_0}^x, \sigma_{i_0}^y, \sigma_{i_0}^z\} \quad (15)$$

where we take $i_0 = \lfloor N/2 \rfloor$ as a generic choice. The set of global operators is formed by the collective spin components

$$A(0) \to \{S_x, S_y, S_z\} \quad (16)$$

where $S_\alpha = \sum_{i=1}^{N} \sigma_i^\alpha / 2$. Clearly, for these choices of single-site and global operators we have $\mu(0) = 1$ as these operators have (initially) only support on size-1 Paulis. Thus,
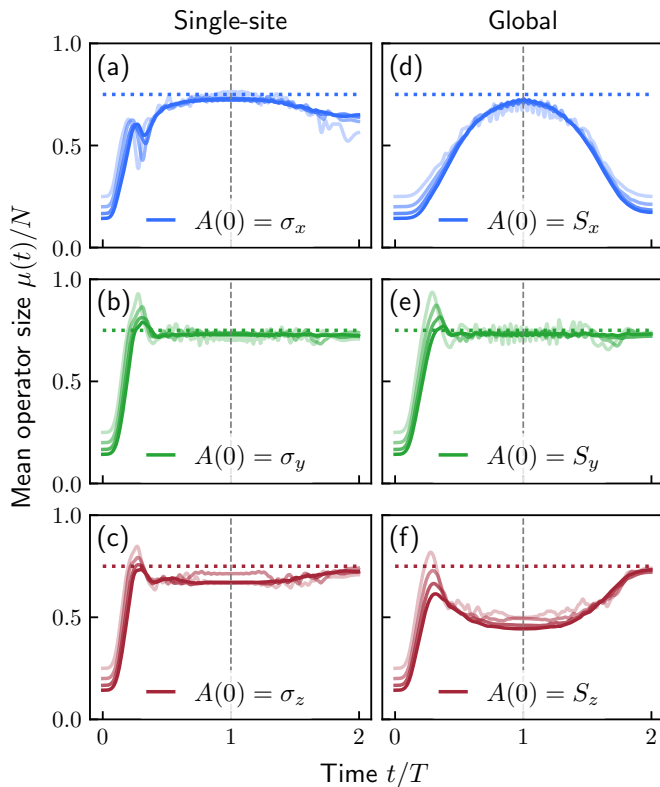
FIG. 6. Normalized mean operator size evolution $\mu(t)/N$, defined in Eq. (14), for different choices of initial operators. Plots (a)-(c) correspond to initial single-site operators shown in Eq. (15), while (d)-(f) to the global operators defined in Eq. (16). Data is shown for system sizes $N = 4, 5, 6, 7$ (light to dark color tones). All cases show evolution under the cyclic driving discussed in Sec. II; dashed vertical lines indicate $t = T$, where the forward ramp ends, and the backward ramp begins. Dotted horizontal lines correspond to the mean operator size expected for Haar random evolution $\mu_{\text{Haar}}/N = 3/4$.

we are interested in analyzing the initial growth and subsequent evolution of the mean operator size under the different types of adiabatic evolution considered in the previous section.

A. Dynamics of local operators

Fig. 6 (a)-(c) shows the evolution of the mean operator size for the set of single-site operators described above. Data is shown for the complete cyclic ramp, meaning that dynamics up to $t/T = 1$ corresponds to the forward ramp from $s(0) = 0$ to $s(T) = 1$, while the subsequent evolution arises from the backwards ramp leading back to $s(2T) = 0$. In all cases, we show data for different system sizes $N = 4, 5, 6, 7$ (light to dark tones). We point out that exact numerical evaluation of the OSD is computationally expensive as it requires to calculate the full operator evolution and then project onto each element of the many-body Pauli basis, which is exponential

in size. The evolution shown in Fig. 6 (a)-(c) indicates that single-site operators grow during the forward adiabatic evolution and become extensive, with support on all the degrees of freedom of the system. Notably, the operator size reached by the end of the forward ramp at $t = T$ is very close to that expected for random evolution, $\sim 3N/4$. Thus, in line with the results in Sec. III and Sec. IV, we see that the adiabatic driving leads to a highly chaotic evolution, in this case witnessed by scrambling in the operator dynamics.

Perhaps more surprisingly, we observe that the operators continue to be extensively delocalized even for $T \leq t \leq 2T$, that is, during the backward ramp. The most striking case is σ_y, where the operator size equilibrates at the value expected for random evolution and shows no sign of reversing ("shrinking") to lower values at the end of the protocol. The evolution of these single-site operators thus starkly contrasts the cyclic evolution expected for states in the low-energy sector. In fact, we find that single-site operators evolve in an *almost* thermal fashion, with effectively irreversible dynamics. This hints at the fact that the evolution of these operators is dominated by the properties of the bulk eigenstates of $H(s(t))$, where adiabaticity is essentially not possible.

B. Dynamics of global operators

As we discussed above, the operator dynamics for the set of single-site Pauli operators shows clear signatures of information scrambling. In particular, we found that the mean operator size dynamics is equivalent to that generated by Haar-random dynamics, meaning that the "gentle" adiabatic drive has a similar effect as one would expect from a thermalizing periodically driven system, or even from a random quantum circuit. However, as we have seen in Sec. IV, the cyclic adiabatic evolution is non-generic and deviations from chaotic evolution are expected. Here we discuss such cases for the operator dynamics.

In Fig. 6 (d)-(f) we display the mean operator size for the global operators $\{S_x, S_y, S_z\}$. The dynamics bears similarities and differences with the evolution of single-site operators. For the forward ramp, $0 \leq t \leq T$, we observe that operator sizes become clearly extensive with values matching those of random operators for S_x and S_y; the case of S_z shows maximum operator size increasing with system size, but clearly deviates from the Haar prediction. From all cases considered, the one that stands out the most is S_x, where we observe that size of S_x shrinks back to ~ 1 during the backward ramp. Thus, we see that the dynamics of S_x reverses back to its initial configuration, although not perfectly. A key aspect here is that S_x is a special operator in this problem, since its proportional to the mixer Hamiltonian, i.e. $H(0) = H(2T) = H_M = 2S_x$. At first sight, the evolution of S_x seen here is consistent with the expectation that the adiabatic evolution should connect the eigen-

states of H_M back to themselves at the end of the cyclic protocol. However, a more detailed inspection reveals that only the eigenstates of S_x near the edges of its spectrum follow this expected evolution, while eigenstates near the bulk undergo mixing evolution. We show this analysis in Appendix A. As evidenced from the results in this section, it suffices that the dominant eigenstates (i.e. those with larger eigenvalues in absolute value) evolve adiabatically for the operator size to shrink back to its original configuration.

VI. DISCUSSION AND OUTLOOK

In this work we have shown that a basic model of a quantum annealer can display clear signatures of quantum ergodicity and scrambling. These features become prominent when one considers the dynamical behavior of these models beyond the low (and high) energy regime. Here, we have analyzed three specific aspects which fall into this criterion: the generation of volume-law entanglement when the system is initialized in a product state which is rotated from the ground state, the random-matrix-like spectral properties of the complete unitary map $U(T)$ describing the annealing dynamics, and the onset of information scrambling as measured by the growth of generic operators in the Heisenberg picture. Furthermore, we have shown that the counterintuitive fact that slow adiabatic drive results in strongly chaotic dynamics is balanced by the existence of clear deviations from chaoticity which are observed when a cyclic adiabatic drive is considered.

Our findings show that a quantum annealing device, originally designed to follow adiabatically low-energy states, could have interesting additional applications if one uses it in a different regime. For instance, achieving scrambling, random-like dynamics can be a useful tool for device benchmarking. In fact, while it is somewhat straightforward to engineer a quantum circuit that scrambles most initial states, it is not so clear how to find a class of models where a subset of initial states thermalize while others do not. A notable example of such models would be those featuring Quantum Many-Body Scars (QMBS) [48], which refer to the existence of anomalous high-energy eigenstates which deviate from the eigenstate thermalization hypothesis description [6, 49, 50]. Systems displaying QMBS can lead to non-thermal dynamics when starting from certain physical states, but evidence suggests that QMBS emerge in fine-tuned models, and are not typically robust (see [51] for exceptions). Our analysis shows that quantum annealers lead to a dynamical process which will scramble most initial states, except for those associated with the low- and high-energy subspaces of H_M. Having an initial-state dependent entanglement growth could be a useful tool for benchmarking quantum devices, as it would allow to vary the hardness of tracking the dynamics with classical methods such as matrix product states.

The emergence of ergodicity in the annealing dynamics can also have negative consequences. For instance, the rather sharp separation between low-energy states (following adiabatic dynamics) and bulk states (following mixing dynamics) shown in Fig. 6 indicates that adiabatic algorithms could have limited scope in the task of preparing excited states.

Beyond its relevance for quantum annealing devices, our study is naturally connected to fundamental aspects of nonequilibrium many-body quantum systems under adiabatic driving. While here we have studied a model defined on a chaotic path (see Fig. 1a), setting $\lambda = 0$ in Eq. (1) would actually render the model integrable for all values of s. In addition, adiabaticity in the bulk of the spectrum could be easier to achieve in such case thanks to the existence of conserved quantities leading to exact crossings in the spectrum. Recent studies have focused on a complimentary model featuring all-to-all interactions, but where the addition of driving leads to quantum chaos signatures [32]. In this vein, we notice that a small $\lambda > 0$ (i.e., a weak integrability breaking) leads to avoided crossings with very small gaps, in fact smaller than in the chaotic regime, which displays level repulsion. The characterization of integrability-to-chaos transition in terms of adiabatic process has also been studied recently [52, 53], and integrable many-body adiabatic dynamics has been shown to impact the proliferation of errors in quantum annealing [34]. In this context, further characterizing the interplay between adiabaticity and (non) integrability in a more general setting stands out as an interesting open problem.

ACKNOWLEDGMENTS

Appendix A: Evolution of entangled states

To complement the results on the evolution of product states discussed in Sec. III, here we consider the evolution of entangled states for both the forward and cyclic ramps. We focus on the family of Dicke states, $\{|D_k^N\rangle\}_{k=0,\ldots,N}$, on the x-basis, i.e., the eigenbasis of H_{M}. Each of the $|D_k^N\rangle$ is the equal superposition of all N-qubit states $|\mathbf{z}\rangle$, where $\mathbf{z}$ is a bitstring of fixed Hamming weight $\mathrm{w}(\mathbf{z}) = k$, with the latter being the number of spin flips required to map $\mathbf{z}$ on to the all-down (all-zeros) string. That is, a state where k spin flips are distributed permutationally
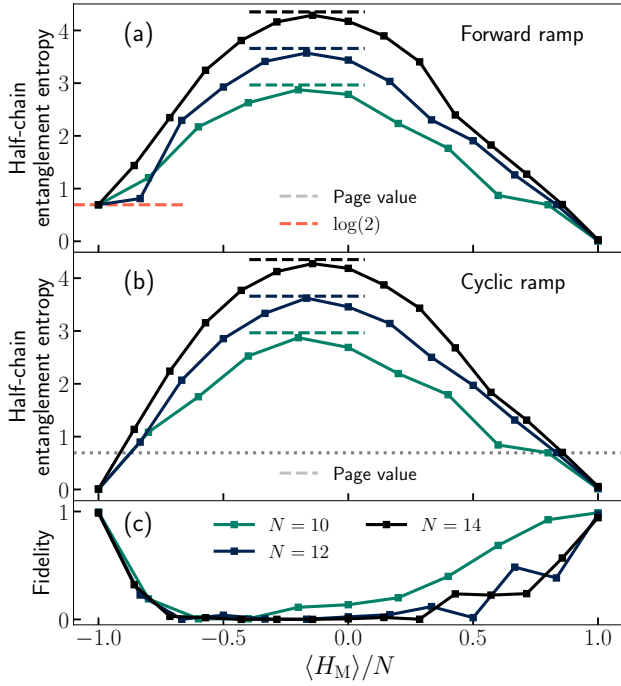
FIG. 7. Adiabatic evolution of Dicke states in the x-basis as a function of their mean energy density $\langle H_{\mathrm{M}} \rangle/N$. (a) Half-chain entanglement entropy of the final state after the forward ramp. (b) Half-chain entanglement entropy of the final state after the cyclic ramp. (c) Final state fidelity after the cyclic ramp. Parameters are: $T = 600$, $\Delta t = 0.05$.

invariant over the N spins. We write

$$|D_k^N\rangle = \binom{N}{k}^{-\frac{1}{2}} \sum_{\mathbf{z}|\mathrm{w}(\mathbf{z})=\mathrm{k}} \mathrm{H}^{\otimes N}|\mathbf{z}\rangle, \qquad \text{(A1)}$$

where H is the Hadamard quantum logic gate. Clearly $H_{\mathrm{M}}|D_k^N\rangle = (-N + k)|D_k^N\rangle$, and the first and last Dicke states correspond to $|D_0^N\rangle = |-\rangle^{\otimes N}$ and $|D_N^N\rangle = |+\rangle^{\otimes N}$.

With the exception of the two extremal states mentioned before and the Dicke states with $k = 1, N-1$, all of the other $|D_k^N\rangle$ have a half-chain entanglement entropy which grows logarithmically with N, $S_A \sim \log(N)$ [54]. In particular, when $k = 1$, $|D_1^N\rangle$ is the N-qubit W state, which has $S_A = \log(2)$. Correspondingly $|D_{N-1}^N\rangle = X^{\otimes N}|D_N^k\rangle$ also has $S_A = \log(2)$.

The results of the adiabatic evolution of Dicke states, i.e., with $|\psi(0)\rangle = |D_k^N\rangle$ are shown in Fig. 7 as function of their mean energy density $\langle H_{\mathrm{M}}\rangle/N$ for three systems sizes $N = 10, 12, 14$ (green, blue, black, respectively). Let us consider first the forward ramp, Fig. 7a shows S_A of the final state for all the Dicke states. Naturally $|D_0^N\rangle = |-\rangle^{\otimes N}$ is mapped to the ground state of H_{P} which can be evidenced by the value $S_A = \log(2)$ (orange dashed line), and the $|D_N^N\rangle = |+\rangle^{\otimes N}$ is mapped to the product state of highest energy of H_{P} with $S_A = 0$. Although there are few Dicke states which seem to be transported to states with $S_A(0) = S_A(T)$, see for instance $|D_{N-1}^N\rangle$ for which we have $S_A(0) = S_A(T) = \log(2)$, there is a general tendency of reaching final states with larger S_A, with those closer to $\langle H_{\mathrm{M}}\rangle/N = 0$ reaching S_A consistent with the Page value for random pure states (colored dashed lines). Finally, we notice that the curve $S_A(\langle H_{\mathrm{M}}\rangle/N)$ is assymetric, implying that Dicke states closer to the top of the energy spectrum suffer less from the effects of the ergodic properties of the forward ramp unitary.

We move now to discuss the results of the cyclic ramp. Both the final state S_A and fidelity are shown in Fig. 7b,c, respectively, as function of $\langle H_{\mathrm{M}}\rangle/N$. We see that the two extremal states of H_{M} are transported back onto themselves. All the other Dicke states are transported onto states of increasing final S_A with $\langle H_{\mathrm{M}}\rangle/N$ reaching values very close to Page value (see dashed lines in Fig. 7b), thus leading to rapidly decreasing fidelity with $\langle H_{\mathrm{M}}\rangle/N$. Interestingly the asymmetry between Dicke states of negative and positive mean-energy is manifested in the final state of the cyclic ramp as well. In particular, those Dicke states of positive mean-energy suffer less from the deleterious effects of the ergodic properties of $U(2T)$ and we observed higher final state fidelities after the cyclic ramp.

[1] A. Rajak, S. Suzuki, A. Dutta, and B. K. Chakrabarti, Quantum annealing: An overview, Philosophical Transactions of the Royal Society A **381**, 20210417 (2023).
[2] T. Albash and D. A. Lidar, Adiabatic quantum computation, Rev. Mod. Phys. **90**, 015002 (2018).
[3] N. V. Vitanov, A. A. Rangelov, B. W. Shore, and K. Bergmann, Stimulated raman adiabatic passage in physics, chemistry, and beyond, Reviews of Modern Physics **89**, 015006 (2017).
[4] E. Farhi, J. Goldstone, and S. Gutmann, A quantum approximate optimization algorithm, arXiv preprint arXiv:1411.4028 (2014).
[5] K. Blekos, D. Brand, A. Ceschini, C.-H. Chou, R.-H. Li, K. Pandya, and A. Summer, A review on quantum approximate optimization algorithm and its vari-

ants, Physics Reports **1068**, 1 (2024).
[6] M. Rigol, V. Dunjko, and M. Olshanii, Thermalization and its mechanism for generic isolated quantum systems, Nature **452**, 854 (2008).
[7] A. Polkovnikov, K. Sengupta, A. Silva, and M. Vengalattore, Colloquium: Nonequilibrium dynamics of closed interacting quantum systems, Rev. Mod. Phys. **83**, 863 (2011).
[8] L. F. Santos and M. Rigol, Onset of quantum chaos in one-dimensional bosonic and fermionic systems and its relation to thermalization, Phys. Rev. E **81**, 036206 (2010).
[9] L. D'Alessio, Y. Kafri, A. Polkovnikov, and M. Rigol, From quantum chaos and eigenstate thermalization to statistical mechanics and thermodynamics, Advances in

Physics **65**, 239 (2016).

[10] M. H. Muñoz Arias, Statistical complexity and the road to equilibrium in many-body chaotic quantum systems, Phys. Rev. E **106**, 044103 (2022).

[11] A. Gubin and L. F Santos, Quantum chaos: An introduction via chains of interacting spins 1/2, American Journal of Physics **80**, 246 (2012).

[12] P. Łydżba, M. Rigol, and L. Vidmar, Entanglement in many-body eigenstates of quantum-chaotic quadratic hamiltonians, Phys. Rev. B **103**, 104206 (2021).

[13] M. Kliczkowski, R. Świętek, L. Vidmar, and M. Rigol, Average entanglement entropy of midspectrum eigenstates of quantum-chaotic interacting hamiltonians, Phys. Rev. E **107**, 064119 (2023).

[14] X. Wang, S. Ghose, B. C. Sanders, and B. Hu, Entanglement as a signature of quantum chaos, Physical Review E—Statistical, Nonlinear, and Soft Matter Physics **70**, 016217 (2004).

[15] P.-Y. Chang, X. Chen, S. Gopalakrishnan, and J. H. Pixley, Evolution of entanglement spectra under generic quantum dynamics, Phys. Rev. Lett. **123**, 190602 (2019).

[16] L. D'Alessio and M. Rigol, Long-time behavior of isolated periodically driven interacting lattice systems, Phys. Rev. X **4**, 041048 (2014).

[17] F. Haake, M. Kuś, and R. Scharf, Classical and quantum chaos for a kicked top, Zeitschrift für Physik B Condensed Matter **65**, 381 (1987).

[18] D. N. Page, Average entropy of a subsystem, Phys. Rev. Lett. **71**, 1291 (1993).

[19] A. Lucas, Ising formulations of many np problems, Frontiers in Physics **2**, 10.3389/fphy.2014.00005 (2014).

[20] S. Ebadi, A. Keesling, M. Cain, T. T. Wang, H. Levine, D. Bluvstein, G. Semeghini, A. Omran, J.-G. Liu, R. Samajdar, X.-Z. Luo, B. Nash, X. Gao, B. Barak, E. Farhi, S. Sachdev, N. Gemelke, L. Zhou, S. Choi, H. Pichler, S.-T. Wang, M. Greiner, V. Vuletić, and M. D. Lukin, Quantum optimization of maximum independent set using rydberg atom arrays, Science **376**, 1209 (2022), https://www.science.org/doi/pdf/10.1126/science.abo6587.

[21] D. Sherrington and S. Kirkpatrick, Solvable model of a spin-glass, Phys. Rev. Lett. **35**, 1792 (1975).

[22] P. Charbonneau, E. Marinari, M. Mézard, G. Parisi, F. Ricci-Tersenghi, G. Sicuro, and F. Zamponi, Spin Glass Theory and Far Beyond (WORLD SCIENTIFIC, 2023) https://www.worldscientific.com/doi/pdf/10.1142/13341.

[23] J. Karthik, A. Sharma, and A. Lakshminarayan, Entanglement, avoided crossings, and quantum chaos in an ising model with a tilted magnetic field, Phys. Rev. A **75**, 022304 (2007).

[24] H. Kim and D. A. Huse, Ballistic spreading of entanglement in a diffusive nonintegrable system, Phys. Rev. Lett. **111**, 127205 (2013).

[25] H. Kim, M. C. Bañuls, J. I. Cirac, M. B. Hastings, and D. A. Huse, Slowest local operators in quantum spin chains, Phys. Rev. E **92**, 012128 (2015).

[26] A. Grabarits, K. R. Swain, M. S. Heydari, P. Chandarana, F. J. Gómez-Ruiz, and A. del Campo, Quantum chaos in random ising networks, arXiv preprint arXiv:2405.14376 (2024).

[27] Y. Y. Atas, E. Bogomolny, O. Giraud, and G. Roux, Distribution of the ratio of consecutive level spacings in random matrix ensembles, Phys. Rev. Lett. **110**, 084101 (2013).

[28] M. V. Berry, Quantal phase factors accompanying adiabatic changes, Proc. R. Soc. Lond. A **392**, 45–57 (1984).

[29] M. Born and V. Fock, Beweis des adiabatensatzes, Zeitschrift für Physik **51**, 165–180 (1928).

[30] T. Kato, On the adiabatic theorem of quantum mechanics, Journal of the Physical Society of Japan **5**, 435 (1950).

[31] H. Yarloo, H.-C. Zhang, and A. E. B. Nielsen, Adiabatic time evolution of highly excited states, PRX Quantum **5**, 020365 (2024).

[32] R. Puebla and F. J. Gómez-Ruiz, Quantum information scrambling in adiabatically driven critical systems, Entropy **26**, 951 (2024).

[33] S. Jansen, M.-B. Ruskai, and R. Seiler, Bounds for the adiabatic approximation with applications to quantum computation, Journal of Mathematical Physics **48** (2007).

[34] B. F. Schiffer, A. F. Rubio, R. Trivedi, and J. I. Cirac, The quantum adiabatic algorithm suppresses the proliferation of errors, arXiv preprint arXiv:2404.15397 (2024).

[35] C. Yi, Success of digital adiabatic simulation with large trotter step, Phys. Rev. A **104**, 052603 (2021).

[36] L. K. Kovalsky, F. A. Calderon-Vargas, M. D. Grace, A. B. Magann, J. B. Larsen, A. D. Baczewski, and M. Sarovar, Self-healing of trotter error in digital adiabatic state preparation, Phys. Rev. Lett. **131**, 060602 (2023).

[37] J. M. Radcliffe, Some properties of coherent spin states, Journal of Physics A: General Physics **4**, 313 (1971).

[38] F. Haake, Quantum signatures of chaos (Springer, 1991).

[39] J. M. Magán, Random free fermions: An analytical example of eigenstate thermalization, Phys. Rev. Lett. **116**, 030401 (2016).

[40] E. Bianchi, L. Hackl, and M. Kieburg, Page curve for fermionic gaussian states, Phys. Rev. B **103**, L241118 (2021).

[41] L. Amico, R. Fazio, A. Osterloh, and V. Vedral, Entanglement in many-body systems, Rev. Mod. Phys. **80**, 517 (2008).

[42] E. Bianchi, L. Hackl, M. Kieburg, M. Rigol, and L. Vidmar, Volume-law entanglement entropy of typical pure quantum states, PRX Quantum **3**, 030201 (2022).

[43] D. A. Roberts, D. Stanford, and A. Streicher, Operator growth in the syk model, Journal of High Energy Physics **2018**, 1 (2018).

[44] D. E. Parker, X. Cao, A. Avdoshkin, T. Scaffidi, and E. Altman, A universal operator growth hypothesis, Phys. Rev. X **9**, 041017 (2019).

[45] Q. Zhuang, T. Schuster, B. Yoshida, and N. Y. Yao, Scrambling and complexity in phase space, Phys. Rev. A **99**, 062334 (2019).

[46] S. Omanakuttan, K. Chinni, P. D. Blocher, and P. M. Poggi, Scrambling and quantum chaos indicators from long-time properties of operator distributions, Physical Review A **107**, 032418 (2023).

[47] T. Schuster and N. Y. Yao, Operator growth in open quantum systems, Physical Review Letters **131**, 160402 (2023).

[48] M. Serbyn, D. A. Abanin, and Z. Papić, Quantum many-body scars and weak breaking of ergodicity, Nature Physics **17**, 675 (2021).

[49] M. Srednicki, Chaos and quantum thermalization, Phys. Rev. E **50**, 888 (1994).

[50] J. M. Deutsch, Quantum statistical mechanics in a closed

system, Phys. Rev. A **43**, 2046 (1991).

[51] A. Lerose, T. Parolini, R. Fazio, D. A. Abanin, and S. Pappalardi, Theory of robust quantum many-body scars in long-range interacting systems, arXiv preprint arXiv:2309.12504 (2023).

[52] M. Pandey, P. W. Claeys, D. K. Campbell, A. Polkovnikov, and D. Sels, Adiabatic eigenstate deformations as a sensitive probe for quantum chaos, Physical Review X **10**, 041017 (2020).

[53] A. V. Varma, A. Vardi, and D. Cohen, Many-body adiabatic passage: Instability, chaos, and quantum classical correspondence, arXiv preprint arXiv:2409.00952 (2024).

[54] M. Kumari and Á. M. Alhambra, Eigenstate entanglement in integrable collective spin models, Quantum **6**, 701 (2022).